Asociación Argentina
de Mecánica Computacional

Mecánica Computacional Vol XXXVI, págs. 1729-1739 (artículo completo)
José G. Etse, Bibiana M. Luccioni, Martín A. Pucheta, Mario A. Storti (Eds.)
San Miguel de Tucumán, 6-9 Noviembre 2018

CORONARY FLOW ESTIMATION FOR THE COMPUTATIONAL ASSESSMENT OF FRACTIONAL FLOW RESERVE

Carlos C. Bulant[a], Pablo J. Blanco[b], Gonzalo D. Maso Talou[b], Alejandro Clausse[a,d], Cristiano G. Bezerra[c], Pedro A. Lemos[c] and Raúl A. Feijóo[b]

[a]*CONICET and Universidad Nacional del Centro, UNICEN, Argentina*

[b]*National Laboratory for Scientific Computing, LNCC/MCTIC, Petrópolis, Brazil*

[c]*Heart Institute, University of São Paulo Medical School, INCOR-FM-USP, São Paulo, Brazil*

[d]*Comisión Nacional de Energía Atómica, CNEA, Argentina*

Keywords: 0D Model, Fractional Flow Reserve, Kalman Filter, Coronary Flow Reserve.

Abstract. Nowadays, fractional flow reserve (FFR) is considered the gold standard technique to assess risk of myocardial ischemia in the presence of coronary artery disease. Moreover, FFR is an invasive procedure, which requires specialized cardiologist and dedicated medical instrumentation, i.e. it is far from being risk free and it is expensive. In this context, a tool to estimate FFR from computational fluid dynamics non-invasively could impact positively the patient experience, reducing economic costs and providing a new diagnostic tool for physicians. Although there are some studies proposing computational solutions for the estimation of FFR, they generally lack of sensitivity analysis of the hemodynamics parameters. In this work we are interested in assessing the effect of coronary flow reserve (CFR) in the outcomes of the numerical simulations of coronary blood flow. To this end we make use of a set of 24 coronary computed tomography angiography (CCTA) images from which the arterial network is segmented and utilized to perform blood flow simulations. The blood circulation is modeled using lumped mathematical representations in a steady state regime, with geometrical features retrieved from the CCTA images. At least one measurement of fractional flow reserve (FFR) is available for each patient, totaling 35 measurements. Some hemodynamic parameters for the simulations were found to be patient specific while others are calibrated with a single general value for all patients. The study focuses on the estimation of CFR that minimizes the difference between the in-vivo FFR measurements and the computational estimations. This strategy may shed light on the underlying mechanisms ruling territorial myocardial resistance.

Copyright © 2018 Asociación Argentina de Mecánica Computacional http://www.amcaonline.org.ar

1 INTRODUCTION

The gold standard tool to quantify functional severity of a coronary artery stenosis is the Fractional Flow Reserve (FFR) index (Tonino et al., 2009). It is calculated as the ratio of post- and pre-stenotic blood pressure measurements under hyperemic conditions. In clinical protocols, FFR < 0.8 indicates that the patient is at risk of suffering myocardial isquemia due to the functional severity of the stenosis.

In recent years, the scientific community specialized in computational hemodynamics incurred in the estimation of FFR through computer simulations. In this context, several approaches using image modalities such as coronary computed tomography angiography (CCTA) (Taylor et al., 2013) and angiography (AX) (Morris et al., 2013) emerged, see (Bulant, 2017) for a comprehensive review. Most of the proposed methods, use 3D models to solve the computational fluid dynamic problem (Taylor et al., 2013), some use 1D models (Itu et al., 2012), but a few solutions were proposed using 0D models (Huo et al., 2012). It is important to remark that the use of 3D models poses several challenges, which range from detailed 3D lumen segmentation procedures and mesh generation to time-consuming numerical simulations in high performance computing facilities. Although 1D simulations are cheaper from the computational point of view, a comprehensive comparison to 3D simulations in the context of FFR is still lacking in the literature. Regarding 0D models, current approaches (Huo et al., 2012) focused on the pressure drop across stenoses, modeling a single artery, and neglecting issues such as patient specific coronary blood flow estimation or flow distribution, which are key, as will be presented in this work.

Generally, the literature addressing the computational estimation of FFR concentrates on comparing a given proposed methodology to the invasive measurements (Bulant, 2017). But little detail is given to the impact of model parameters in the simulation outcome. Studying the sensitivity of the method to model parameters is crucial to understand the estimation errors and improve the method. Empirical analysis requires to perform several computer simulations varying the parameters values. In such context, cheap computational models, like the 0D, allows to efficiently analyze different scenarios, providing physiologically reasonable coarse descriptions of the hemodynamics in vascular networks.

The goals of this work are: (i) Present a 0D model to computationally estimate the fractional flow reserve, FFR_{CE}, from CCTA images and patient data; (ii) Validate the model against invasive measurement, FFR_{inv}; (iii) Assess the impact of the coronary flow reserve, CFR, on the computation of FFR_{CE} by data assimilation using Kalman filter.

2 MATERIALS

The study sample was constructed from patients with suspected chronic coronary disease who underwent multimodal evaluation with CCTA and a posterior FFR_{inv} measurement. The study protocol was approved by the ethics committee of the Heart Institute and the Sírio-Libanês Hospital, both in São Paulo, Brazil. Overall, 35 vessels of 24 patients were assessed using FFR_{inv}. Baseline clinical and lesions characteristics are outlined in Tables 1 and 2.

3 METHODS

3.1 From images to arterial models

Imaging data were acquired following standardized image acquisition protocols, at the Instituto do Coração (InCor) and Hospital Sírio-Libanês, São Paulo, Brazil.

Copyright © 2018 Asociación Argentina de Mecánica Computacional http://www.amcaonline.org.ar

Baseline clinical characteristic	**Patient sample** ($n = 24$)
Age, yrs	61±9
Male	21 (87)
BMI, kg/m2	28±3
Weight, Kg	85±15
Height, cm	174±10
HR, bpm	70±8
SP, mmHg	113±13
DP, mmHg	68±10
MP, mmHg	84±10
Circulation Dominance	
Right	22 (92)
Left	1 (4)
Co	1 (4)

Table 1: Summary of patient data, the mean ± SD, or n (%), are reported. Body mass index (BMI), heart rate (HR), diastolic, systolic and mean pressures (DP, SP and MP).

Baseline lesion characteristic	**Vessel sample** ($n = 35$)
LAD	21 (60)
LCX	6 (17)
RI	1 (3)
OM	1 (3)
RCA	6 (17)
FFR_{inv}	0.88±0.08 (0.71, 0.99)

Table 2: Summary of lesions, the mean ± SD (min, max), or n (%), are reported.

	Circ. Dominance	**LAD**	**LCx**	**RCA**	**RI**
RI not present	**Right**	60	22	18	0
	Left	60	30	10	0
	Co	60	24	16	0
RI present	**Right**	57	10	18	15
	Left	60	15	10	15
	Co	59	10	16	15

Table 3: Percentage of the Q_T at the inlet of each major artery.

Segmentation of CCTA images is achieved using the methodology detailed in Bulant et al. (2017), based on level sets and colliding front techniques (Antiga et al., 2008). This procedure results in a triangulated raw surface of the coronary tree. Such mesh is smoothed and used to construct the arterial tree centerline following Antiga et al. (2003).

Centerlines are polyline structures that retain: arterial length, spatial disposition and vessel cross-sectional radius. Centerlines are post-processed to account for: bifurcation mask defining the arterial ostium per artery; stenosis mask, defining lesioned regions, manually marked by an specialist; label defining the anatomical name of each artery, see Bulant et al. (2017) for details.

3.2 Blood flow model

The simulations are performed using the patient-specific centerline as the geometric substrate for the numerical model. Such structure comprises the key information required by the model to perform the simulation: (a) the topological connectivity of the arterial segments, through their branching points; (b) the point-wise information of the arterial radius, r_i, $i = \{1, ..., N\}$, with N the number of centerline points (a computational node per point is considered); (c) the root point, which is the network inlet at the aortic root, I; and the network outlets O_m, $m = 1, ..., N_O$; (d) the mask identifying nodes corresponding to the stenotic lesions.

A steady state 0D model is used to describe the incompressible flow of a Newtonian fluid in non-compliant vessels. The stenosis model proposed by Young and Tsai (1973) is used at locations identified as stenotic. The blood pressure (P_i) and the blood flow rate Q_i are computed at each computational node (i). The governing 0D equations are detailed below.

The standard mass conservation and pressure continuity junction model are used at each bifurcation point, where node i branches into nodes j and k, yielding

$$\begin{cases} Q_i = Q_j + Q_k, \qquad \text{and} \qquad P_i = P_j = P_k. \end{cases} \tag{1}$$

Given an arterial segment containing M points, $M - 1$ lumped parameter elements are used. For each element, the mass conservation and the hydraulic analogue of the Ohm's law are

Copyright © 2018 Asociación Argentina de Mecánica Computacional http://www.amcaonline.org.ar

considered. Then, for an element formed by nodes i and $i+1$, the equations are

$$\begin{cases} Q_{i+1} = Q_i, & \text{and} \quad Q_{i+1} = \dfrac{P_i - P_{i+1}}{R_{i,i+1}}, \end{cases} \tag{2}$$

where, the resistance to the flow at each segment is modeled with an extension of Poiseuille's law for tubular segments featuring tapering

$$R_{i,i+1} = \frac{8\mu L}{3\pi}\left[\frac{1}{r_i^3 r_{i+1}} + \frac{1}{r_i^2 r_{i+1}^2} + \frac{1}{r_i r_{i+1}^3}\right]. \tag{3}$$

where L is the element length, μ is the blood viscosity, and r_i, r_{i+1} are the radii at nodes i and $i+1$. Note that for a vessel with uniform radius, i.e. $r_i = r_{i+1}$, equation (3) reduces to the classic Poiseuille's formula.

Each stenotic region of the tree is replaced with a lumped parameter model proposed by Young and Tsai (1973), for which we have

$$\begin{cases} Q_{i+1} = Q_i, & \text{and} \quad P_i - P_{i+1} = K_v \dfrac{\mu}{D}\dfrac{Q_i}{A} + K_t \dfrac{\rho}{2}\left[\dfrac{A}{A_s} - 1\right]^2 \dfrac{Q_i^2}{A^2}, \end{cases} \tag{4}$$

where ρ is the blood density, Q_i and A (D the diameter) are the flow and lumen area in the unobstructed part of the vessel, A_s is the minimum stenosis area, K_v and K_t are model parameters characterizing viscous and turbulent losses, respectively. These parameters are chosen following Seeley and Young (1976) as

$$\begin{cases} K_t = 1.52, & \text{and} \quad K_v = 32\dfrac{0.83L_s + 1.64D_s}{D}\left[0.75\left(\dfrac{A}{A_s}\right) + 0.25\right]^2, \end{cases} \tag{5}$$

where L_s is the lesion length and D_s is the minimum cross-sectional diameter of the stenosis.

Regarding boundary conditions, the pressure and flow rates, are prescribed at the inlet and outlets, respectively:

$$\begin{cases} P_I = P_{\text{ao}}, & Q_{O_m} = \bar{Q}_{O_m} \quad m = 1, \ldots, N_O, \quad \text{and} \quad Q_T = \displaystyle\sum_{m=1}^{N_O} \bar{Q}_{O_m}. \end{cases} \tag{6}$$

The pressure at the inlet is set to the mean aortic pressure (P_{ao}), while the total coronary flow Q_T is the sum of outflows ($\bar{Q}_{O_m}$). Each of which is set to the value given by an adaptation of the Murray's law, which relates the flow rate of a segment to its inlet radius, see Section 3.2.1.

In the numerical implementation, Eq. (4) is linearized using fixed-point iterations. The resulting real linear system of equations is solved using `LAPACK dgles` function through a QR factorization within a custom `C++` source code.

3.2.1 Flow distribution

The widely known Murray's law Murray (1926), relates (i) flow to vessel diameter and (ii) diameter of vessels sharing a bifurcations through a power law. According to the seminal work of Murray Murray (1926), the optimal branching structure of a vascular tree is theoretically equivalent to $Q = \beta r^\gamma$ with $\gamma = 3$. Numerical studies have shown a value of $\gamma = 2.66$ for vascular networks constructed with the CCO method Blanco et al. (2013) in which the total flow rate is proportional to the volume of the vascular territory.

Copyright © 2018 Asociación Argentina de Mecánica Computacional http://www.amcaonline.org.ar

In this work, given the total flow Q_T and the arterial centerline for a given patient, the flow distribution is estimated using the so-called proximal Murray flow distribution (PMD), introduced in Bulant (2017). Briefly, the PMD method was designed to account for tapering in long segments lacking side branches, a situation which is frequently encountered in models constructed from CCTA images with low-quality. In such context, Murray's law hypothesis (constant section diameter per segment and homogeneous wall shear stresses) are not fulfilled.

In practice, for a given arterial tree model obtained proximal CCTA segmentation, radii of arterial segments are more reliable than terminal radii, because of technical limitations such as image resolution and noise. Moreover, the absence of small side branches and associated sub-trees in long arterial segments results in an artificial tapering, directly impacting the flow distribution, when compared to that calculated using all outlet radii only (classic Murray's law). In turn, if Murray's law is recurrently used at each branching point, a more realistic flow at the inlet of large-proximal branches for truncated networks should be expected.

Then, the PMD strategy requires to travel through a coronary network from the aortic root down to the terminals. Starting with the Q_T, at each junction with N_b branches, the algorithm computes the outflow per branch ($\mathcal{Q}_b$) using the ostium radius of each branch (r_b) and the inflow Q_{in} for the junction, this is

$$\left\{ \mathcal{Q}_b = \beta r_b^{\gamma} \qquad b = 1, \ldots, N_b, \qquad \text{and} \qquad \beta = Q_{in} \left(\sum_{b=1}^{N_b} r_b^{\gamma} \right)^{-1} . \right. \tag{7}$$

Note that the method can easily be adapted to account for flow distribution restrictions in specific branches. Exploiting such property, we introduce physiological restrictions such that the flow at the inlet of the main arteries respect the proportions detailed in Table 3.

3.3 Model parameters

In order to perform a computer simulation of the coronary blood flow, two physiological parameters are needed: (i) pressure at the root of the arterial tree, P_a; (ii) total flow rate to be distributed among the outlets, Q_T. The strategy used to estimate such parameters in a patient specific manner is detailed below.

As for the flow distribution method used to determine the outlet boundary conditions, the Murray exponent γ is fixed to $\gamma = 2.66$ for all patients and the patient circulation dominance (right, left or co) is known for each patient. Regarding the mathematical model, the stationary 0D model employed in this work only depends on the blood density and dynamic viscosity. Specifically, we use $\rho = 1.05$ g/cm^3 and for large arteries, $\mu = 0.04$ P, for all patients.

3.3.1 Patient specific parameters

The mean aortic root pressure at rest, MP, is estimated from noninvasive measurements of systolic (SP) and diastolic (DP) pressures at rest. Since FFR is measured under myocardial induced hyperemia, we call the mean aortic root pressure at hyperemia P_a, and is estimated as

$$P_{\text{ao}} = \text{MP} + \Delta, \qquad \text{MP} = \frac{2\text{DP} + \text{SP}}{3}. \tag{8}$$

Where Δ is the effect of intra-coronary ($\Delta = -3.8$) or intra-venous ($\Delta = 4.4$) administration of adenosine, as reported in Bulant (2017). Only one patient of the sample received intra-venous administration. For the patient sample, the average hyperemic aortic pressure value (P_{ao}), as calculated from Eq. (8), was 79.7±10.4 mmHg, in the range (61.2, 98.2) mmHg.

Copyright © 2018 Asociación Argentina de Mecánica Computacional http://www.amcaonline.org.ar

Then, the resting coronary blood flow (RCBF) is assumed to be 4.5% of the cardiac output (CO) Guyton and Hall (2006), which is estimated from non-invasive patient data as follows

$$\begin{aligned} \text{RCBF} &= 0.045 \times \text{CO}, \qquad \text{CO} = \frac{\text{HR} \times \text{SV}}{1000}, \\ \text{SV} &= (0.49 \times (\text{SP} - \text{DP}) + 0.30 \times \text{A} + 7.11) \times \\ &\quad (0.013 \times \text{W} - 0.007 \times \text{A} - 0.004 \times \text{HR} + 1.307), \end{aligned} \tag{9}$$

where HR is the heart rate (in beats/s), SV is the stroke volume (in ml/beat), which is estimated following de Simone and others (1999) from the diastolic and systolic pressures (DP and SP, in mmHg), the age of the patient (A, in years) and its weight (W ,in Kg).

For the study sample, the estimated RCBF is 4.19 ± 0.67 ml/s, in the range (2.89, 5.51) ml/s, which is in the physiological range (4.5 ± 1.37 ml/s) reported by Sakamoto et al. (2013).

Coronary flow reserve (CFR) is defined as the ratio between hyperemic and resting blood flow. Therefore, the hyperemic flow used in the simulations is $Q_T = \text{CBF} = \text{CFR} \times \text{RCBF}$. In nonischemic human coronary arteries, CFR mean value is ~ 2.6 (Johnson et al., 2012). Previous works that aimed to estimate FFR computationally, model hyperemia by reducing terminal resistances by a factor of 4.5 (Taylor et al., 2013), based on Wilson et al. (1990). This work focuses in the data assimilation problem targeting the estimation of CFR values for CFD simulations in patients that underwent the FFR procedure.

3.4 Reduced order unscented Kalman filter

For a given set of observation $Z = [\text{FFR}_{\text{inv}}{}^1, \text{FFR}_{\text{inv}}{}^2, \ldots, \text{FFR}_{\text{inv}}{}^N]$ corresponding to N invasive FFR measurements and the non-linear operator f that computes the fields P and Q for the S arterial models, i.e. one per patient, with parameters $\Gamma = [\Gamma^1, \Gamma^2, \ldots, \Gamma^S]$ –using previously introduced hemodynamic model–, the Kalman filter is formulated as follows

1. Generation of spherical sigma-points $\sigma_i^{(n)}, i = 1, \ldots, N+1$ with their corresponding weights $w^{(i)}$ (see Julier (2003)) and initialization of the variables

$$\mathbf{R}_0 = \sigma_{\text{FFR}_{\text{inv}}} \mathbf{I}_{NN}; \quad \mathbf{L}_0 = \begin{bmatrix} \mathbf{L}_0^{\mathbf{X}} \\ \mathbf{L}_0^{\theta} \end{bmatrix} = \begin{bmatrix} \mathbf{0}_{\mathbf{X}} \\ 1 \end{bmatrix}; \quad \mathbf{U}_0^{-1} = [\sigma_{\hat{\theta}}], \tag{10}$$

$$X_0^a = [\hat{X}_0^+, \hat{\theta}_0^+]^T = [\mathbf{0}_{\mathbf{X}}, \hat{\theta}_0]^T, \tag{11}$$

$$\mathbf{P}_0^+ = \mathbf{L}_0 \mathbf{U}_0^{-1} \mathbf{L}_0^T, \tag{12}$$

where $\hat{\theta}_k$ is the CFR estimate at the k-th filter iteration, $\sigma_{\text{FFR}_{\text{inv}}}$ is the uncertainty of the invasive measurements and $\sigma_{\hat{\theta}}$ is the uncertainty of the CFR parameter. The operator $\mathbf{0}_{\mathbf{X}}$ denotes a column vector of 0's with one element for each degree of freedom across all the hemodynamic simulations. $\hat{X}_0^+$ and $\hat{\theta}_0^+$ are the initial values for P and Q fields and CFR estimate, respectively.

Copyright © 2018 Asociación Argentina de Mecánica Computacional http://www.amcaonline.org.ar

2. The *prediction* step

$$\begin{aligned}
\hat{X}_{k-1}^{(i)} &= \hat{X}_{k-1}^{+} + \mathbf{L}_{k-1}^{X}\sqrt{\mathbf{U}_{k-1}^{-1}}\,\sigma_i^{(n)}, \quad i=1,\dots,N+1,\\
\hat{\theta}_{k-1}^{(i)} &= \hat{\theta}_{k-1}^{+} + \mathbf{L}_{k-1}^{\theta}\sqrt{\mathbf{U}_{k-1}^{-1}}\,\sigma_i^{(n)}, \quad i=1,\dots,N+1,\\
\begin{bmatrix}(\hat{X}_k^{(i)})\\(\hat{\theta}_k^{(i)})\end{bmatrix} &= f\Big(\begin{bmatrix}(\hat{X}_{k-1}^{(i)})\\(\hat{\theta}_{k-1}^{(i)})\end{bmatrix},\Gamma\Big), \qquad \hat{Z}_k^{(i)} = h\Big(\hat{X}_k^{(i)},\Gamma\Big),\\
\hat{X}_k^{-} &= \sum_{i=1}^{N+1} w^{(i)}\hat{X}_k^{(i)}, \quad \hat{\theta}_k^{-} = \sum_{i=1}^{N+1} w^{(i)}\hat{\theta}_k^{(i)}, \quad \hat{Z}_k = \sum_{i=1}^{N+1} w^{(i)}\hat{Z}_k^{(i)}.
\end{aligned} \tag{13}$$

where h is the post-processing operator that estimates the computational FFRs based on the properties Γ and the (P,Q) fields contained in $\hat{X}_k^{(i)}$.

3. The *correction* step

$$\begin{aligned}
\mathbf{L}_k^X &= \hat{\mathbf{X}}_k^{(*)}\mathbf{D}_w(\boldsymbol{\sigma}^{(*)})^T, \quad \mathbf{L}_k^\theta = \hat{\boldsymbol{\theta}}_k^{(*)}\mathbf{D}_w(\boldsymbol{\sigma}^{(*)})^T,\\
\{\mathbf{HL}\}_k &= \hat{\mathbf{Z}}_k^{(*)}\mathbf{D}_w(\boldsymbol{\sigma}^{(*)})^T, \quad \mathbf{P}_w = \boldsymbol{\sigma}^{(*)}\mathbf{D}_w(\boldsymbol{\sigma}^{(*)})^T,\\
\mathbf{U}_k &= \mathbf{P}_w + \{\mathbf{HL}\}_k^T\mathbf{R}_k^{-1}\{\mathbf{HL}\}_k,\\
\hat{X}_k^{+} &= \hat{X}_k^{-} + \mathbf{L}_k^X\mathbf{U}_k^{-1}\{\mathbf{HL}\}_k^T\mathbf{R}_k^{-1}\Big(Z-\hat{Z}_k\Big),\\
\hat{\theta}_k^{+} &= \hat{\theta}_k^{-} + \mathbf{L}_k^\theta\mathbf{U}_k^{-1}\{\mathbf{HL}\}_k^T\mathbf{R}_k^{-1}\Big(Z-\hat{Z}_k\Big).
\end{aligned} \tag{14}$$

The matrices $\boldsymbol{\sigma}^{(*)}, \hat{\mathbf{X}}_k^{(*)}, \hat{\mathbf{Z}}_k^{(*)}, \hat{\boldsymbol{\theta}}_k^{(*)} \in \mathbb{R}^{N\times(N+1)}$, whose columns are $\sigma^{(i)}, \hat{X}_k^{(i)}, \hat{Z}_k^{(i)}, \hat{\theta}_k^{(i)}$, with $i=1,\dots,N+1$, respectively. $\mathbf{D}_w \in \mathbb{R}^{(N+1)\times(N+1)}$ is a diagonal matrix with values $D_{ii}=w^{(i)}, i=1,\dots,N+1$, i.e., the sigma-point weights.

4. If $\frac{\|Z_k - Z_{k-1}\|}{\|Z_{k-1}\|} > \epsilon$ or $k<K$ go to step 2 and $k=k+1$. Otherwise $\hat{\theta}_k^{+}$ is the CFR estimate.

For the following experiments the relative absolute error was $\epsilon = 10^{-4}$, the maximum number of iterations was K=500, the initial guess was CFR=2.6 and the filter uncertainties were set to $\sigma_{\text{FFR}_{\text{inv}}}$=0.001 (corresponding to the precision of the FFR equipment) and $\sigma_{\hat{\theta}}$=0.5. Parameter uncertainty was empirically chosen to deliver the lowest disagreement, i.e., $Z-\hat{Z}_k$.

3.5 Experimental settings

In order to gain insight about the impact of the CFR on the computation of FFR_{CE}, three study cases were designed. The rest of the parameters were fixed for all scenarios, and computed in a patient specific manner as follows: (a) the hyperemic inlet pressure, P_{ao} is estimated following Eq. (8); (b) the resting coronary blood flow, RCBF, is estimated following Eq. (9); (c) given an arterial tree, the flow distribution per outlet, can be estimated in terms of percentages of a normalized total inflow of 1 ml/s, and then automatically adapted for a given Q_T. Then, the CFR, and consequently the hyperemic flow Q_T, for each scenario is calculated as follows:

Experimental setting #1 (E1): The CFR value is set to 2.6 for all the patients, following reported values in the specialized literature (Johnson et al., 2012).

Experimental setting #2 (E2): The CFR value for all patients is the same, and it is estimated by the Kalman filter.

Experimental setting #3 (E3): The CFR value for each patient is estimated by the Kalman filter in a separate manner.

Copyright © 2018 Asociación Argentina de Mecánica Computacional http://www.amcaonline.org.ar

4 RESULTS

Simulations were performed in a personal computer consisting of an Intel(R) Core(TM) i7-7700 CPU @ 3.60GHz with 32 GB of (DDR4) RAM. The average time to solve a 0D simulation was 156 ± 100 s. Meshes contained an average of 1453 ± 309 computational nodes. For experiment E2, a total of 8 Kalman iterations were performed and the filter error was ≈ 0.4. Regarding E3, the mean number of Kalman iterations was 289 ± 221 in the range (9, 500) iterations and the filter error was 0.02 ± 0.03 (0, 0.11).

Table 4 presents a statistical summary of the results for all scenarios. When the Kalman filter is used to estimate one CFR for all patients, i.e. E2, the value obtained was CFR=2.4. This results in the same mean error (ε=FFR_{inv}-FFR_{CE}) than the baseline E1, but with slightly lower variance. Also, E2 reduces the range of values estimated for FFR_{CE}. In turn, when the CFR is estimated in a patient specific manner using the Kalman filter, i.e. E3, the mean error drops to 0.00 ± 0.03. Although the range of ε is the smallest for E3, there are still some out-layers. Such extreme values correspond to patients with FFR_{inv} measurements in more than one artery. Particularly, with low FFR_{inv} in the RCA or LCx and other in the LAD. In these contexts, considering the flow distribution at the ostium of the major arteries, Table 3, and the fact that the method estimates one CFR value for the complete arterial tree, the Kalman filter converges to large CFR values, which for 3 cases was out of the physiological range $[1, 6]$ (Johnson et al., 2012)). For one patient, with one measurement in the RCA (FFR_{inv}=0.97), the estimated CFR value was 7.81, although the RCBF was in the range of physiological values, the flow distribution clearly forced the exaggerated value of CFR. In another patient, with one measurement in the LAD (FFR_{inv}=0.72), the CFR estimation resulted in 7.28, although the RCBF was physiologically consistent, and that the distribution granted 60% at the LAD inlet, the simulation resulted in a large CFR value. These cases illustrate the importance of considering territory-specific CFR estimation.

Figure 1 displays scatter and Bland-Altman plots, and Table 5 presents the predictive capabilities for each experimental setting. On the $n = 35$ available measurements, the prevalence of $FFR_{inv} < 0.8$ is 20%. Estimating the CFR for all patients, i.e. E2, improves the overall predictive indexes, when compared to E1, by slightly increasing the true negative detection, which is consistent with the fact that the CFR is reduced from 2.6 to 2.4. Note that, for E3, although some FFR_{CE} values feature a difference of almost 10%, they are correctly classified, resulting in a perfect classification. Figure 2 shows the 3D model of a specific-patient, the corresponding centerline and the solutions obtained for the E1 and E3 experimental settings. For such patient, the $FFR_{inv} = 0.89$ and the $FFR_{CE}^{E1} = 0.78$ and $FFR_{CE}^{E3} = 0.89$, with CFR 2.6 and 1.35.

In terms of significant ($p < 0.05$) linear correlations between FFR_{CE}, FFR_{inv}, ε, RCBF, CFR and CBF it was found that: (a) For E1 and E2, $r(FFR_{CE}, \varepsilon)$ was -0.52 and -0.43 respectively, indicating that the ε increased for smaller values of FFR_{CE}; (b) For E2, it was found that $r(FFR_{inv}, \varepsilon) = 0.34$, which states that the ε increased as FFR_{inv} increased. (c) For E3, it was found that $r(\text{RCBF}, \text{CBF}) = 0.34$ indicating that the CBF tends to increase as the RCBF increases. (d) Since $\text{CBF} = \text{CFR} * \text{RCBF}$, the correlation between RCBF and CBF was 1 in E1 and E2, and 0.97 in E3. (e) There was no significant correlation between RCBF and CFR.

5 DISCUSSIONS

The objective of this pilot study was to develop a computational infrastructure allowing parameter estimation through the Kalman filter in the context of the computational assessment of FFR through 0D models. Particularly, this work focused in the analysis of the CFR. It was found

Copyright © 2018 Asociación Argentina de Mecánica Computacional http://www.amcaonline.org.ar

Exp.	FFR_{CE} ($n = 35$)	ε ($n = 35$)	CFR ($n = 24$)	CBF ($n = 24$)
E1	0.89±0.09 (0.67, 0.99)	-0.02±0.07 (-0.18, 0.13)	2.6 ±0.00 (2.60, 2.60)	10.9±1.73 (7.51, 14.3)
E2	0.9 ±0.09 (0.70, 0.99)	-0.02±0.06 (-0.19, 0.11)	2.4 ±0.00 (2.40, 2.40)	10.1±1.59 (6.95, 13.2)
E3	0.88±0.08 (0.71, 0.97)	0.00±0.03 (-0.10, 0.05)	4.05±2.56 (1.35, 9.92)	17.1±11.5 (4.78, 44.4)

Table 4: Simulation results, the mean ± SD (min, max) values are reported for FFR_{CE}, the error (ε =FFR_{inv}- FFR_{CE}), the resting coronary blood flow (RCBF), the coronary flow reserve (CFR) and the resulting coronary blood flow (CBF or Q_T).

Exp.	AUC	ACC	SEN	SPE	PPV	NPV	$r^{\dagger}$
E1	0.83	0.80	0.43	0.89	0.50	0.86	0.70
E2	0.84	0.86	0.43	0.96	0.75	0.87	0.70
E3	1.00	1.00	1.00	1.00	1.00	1.00	0.94

Table 5: Predictive capabilities for each setting. The prevalence of FFR_{inv} in the $n = 35$ measurements is 20%. The Area under the ROC curve (AUC), accuracy (ACC), sensitivity (SEN), specificity (SPE), positive predictive value (PPV), negative predictive value (NPV) and the Pearson's correlation coefficient (r). † Stands for $p < 0.01$

that under the assumptions presented here, the use of one CFR value for all patients resulted in reasonable predictive capabilities, with low true positive prediction rates (SEN, PPV). Also, estimating a patient specific CFR substantially improves predictive capabilities, and in 79% of cases results in physiological values. In three patients with more than one FFR_{inv} measurements, the proposed methodology resulted in non-physiological CFR values, which points out towards the need for territory-specific CFR estimation. Those cases have a low FFR_{inv} measure in the RCA or LCx, and another measure in another artery. Then, the large CFR values are explained by the fact that the flow distribution criterion forces the total inflow to the RCA and LCx ostia to be lower than 20% of the total CBF en some cases. In turn, for two patients with one measurement each, the CFR estimation was out of the physiological range. In those cases, the RCBF was slightly smaller than the physiological mean, and in one case the interrogated artery was the RCA and in other the LAD. Then, in the first case a correction of the flow distribution may solve the problem, while in the other it may be necessary to adapt also the RCBF estimation.

Such results suggest: (a) patient specific CFR is important to correctly compute FFR_{CE}; (b) a formula to estimate the CFR per patient should be developed, as for the RCBF; (c) the flow distribution criterion needs revision to achieve physiological CFR values in all cases.

From the modeling point of view, the limitations are those inherent to the nature of 0D models, which have to be ultimately validated against 3D simulations. Such comparison would allow us to quantify the error introduced by such reduced order modeling approach. Future works will focus on: (i) the construction of the CFR formula based on clinical and anatomical patient-specific landmarks; (ii) the improvement of the flow distribution criterion based on territory features; (iii) a rigorous comparison of the 0D against 3D and 1D models.

ACKNOWLEDGEMENTS

The support of Brazilian agencies CNPq and FAPERJ is gratefully acknowledged.

REFERENCES

Antiga L. et al. Computational geometry for patient-specific reconstruction and meshing of blood vessels. *IEEE Trans Med Imaging*, 22(5):674–684, 2003.

Antiga L. et al. An image-based modeling framework for patient-specific computational hemodynamics. *Medical & Biological Engineering & Computing*, 46(11):1097–1112, 2008.

Blanco P., Queiroz R., and Feijóo R. A computational approach to generate concurrent arterial networks in vascular territories. *Int J Numer Method Biomed Eng*, 29:601–614, 2013.

Copyright © 2018 Asociación Argentina de Mecánica Computacional http://www.amcaonline.org.ar

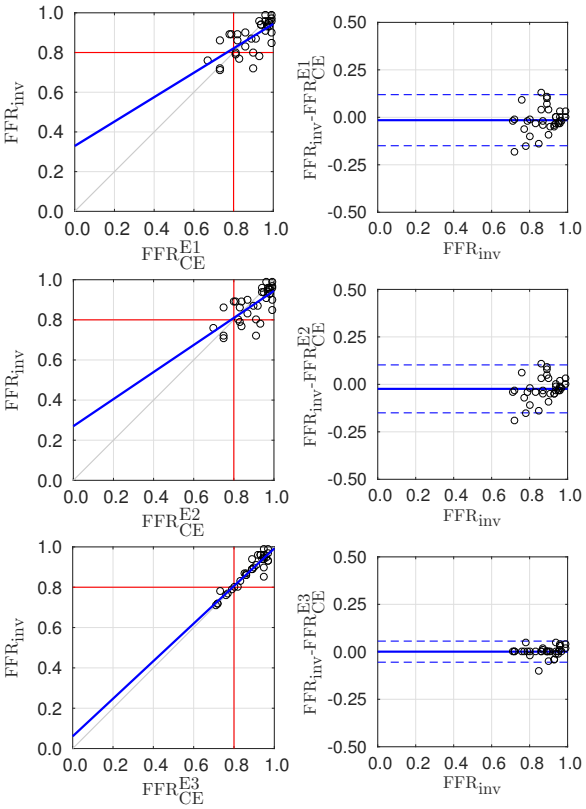

Figure 1: Scatter and Bland-Altman plots comparing FFR_{inv} and FFR_{CE} for each Experimental setting. From left to right, the E1, E2 and E3 experiments.

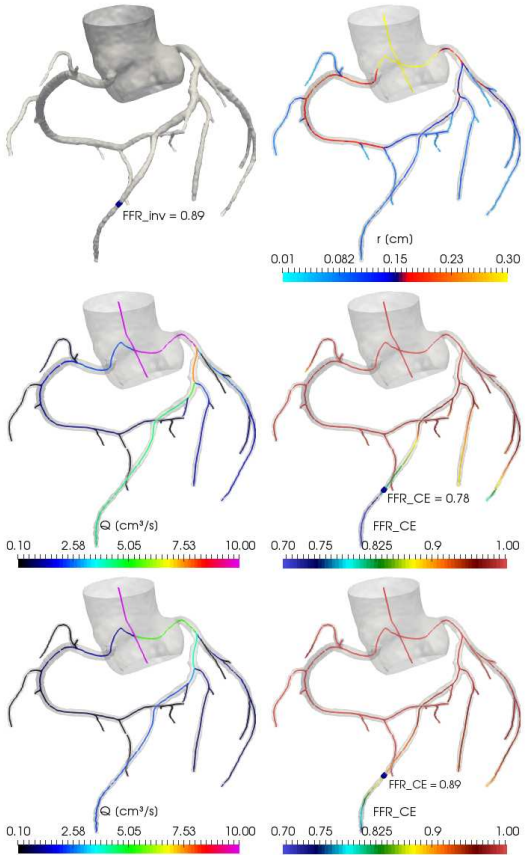

Figure 2: Results for a random patient. First row presents the segmented mesh and the centerline. Solutions of E1 and E3 (mid and last rows), in terms of flow and FFR_{CE}.

Copyright © 2018 Asociación Argentina de Mecánica Computacional http://www.amcaonline.org.ar

Bulant C.A. Computational models for the geometric and functional assessment of the coronary circulation. 2017.

Bulant C.A. et al. A computational framework to characterize and compare the geometry of coronary networks. *Int J Numer Method Biomed Eng*, 33(3):e02800, 2017.

de Simone G. et al. Stroke volume/pulse pressure ratio and cardiovascular risk in arterial hypertension. *Hypertension*, 33(3):800–805, 1999.

Guyton A.C. and Hall J.E. *Textbook of medical physiology*. Elsevier Saunders, Philadelphia, 11th ed edition, 2006.

Huo Y. et al. A validated predictive model of coronary fractional flow reserve. *Journal of the Royal Society, Interface / the Royal Society*, 9(71):1325–1338, 2012.

Itu L. et al. A patient-specific reduced-order model for coronary circulation. In *Biomedical Imaging (ISBI), 2012 9th IEEE International Symposium on*, pages 832–835. IEEE, 2012.

Johnson N.P. et al. Is Discordance of Coronary Flow Reserve and Fractional Flow Reserve Due to Methodology or Clinically Relevant Coronary Pathophysiology? *JACC: Cardiovascular Imaging*, 5(2):193–202, 2012.

Julier S.J. The spherical simplex unscented transformation. In *American Control Conference, 2003. Proceedings of the 2003*, volume 3, pages 2430–2434. IEEE, 2003.

Morris P.D. et al. Virtual Fractional Flow Reserve From Coronary Angiography: Modeling the Significance of Coronary Lesions: Results From the VIRTU-1 Study. *JACC Cardiovasc Interv*, 6(2):149 – 157, 2013.

Murray C.D. The physiological principle of minimum work: I. The vascular system and the cost of blood volume. *Proc. Natl. Acad. Sci. U.S.A.*, 12(3):207, 1926.

Sakamoto S. et al. Relation of Distribution of Coronary Blood Flow Volume to Coronary Artery Dominance. *The American Journal of Cardiology*, 111(10):1420–1424, 2013.

Seeley B.D. and Young D.F. Effect of geometry on pressure losses across models of arterial stenoses. *Journal of biomechanics*, 9(7):439–448, 1976.

Taylor C.A. et al. Computational Fluid Dynamics Applied to Cardiac Computed Tomography for Noninvasive Quantification of Fractional Flow Reserve. *J. Am. Coll. Cardiol.*, 61(22):2233–2241, 2013.

Tonino P.A.L. et al. Fractional flow reserve versus angiography for guiding percutaneous coronary intervention. *The New England journal of medicine*, 360(3):213–224, 2009.

Wilson R.F. et al. Effects of adenosine on human coronary arterial circulation. *Circulation*, 82(5):1595–1606, 1990.

Young D.F. and Tsai F.Y. Flow characteristics in models of arterial stenoses. I. Steady flow. *Journal of biomechanics*, 6(4):395–410, 1973.

Copyright © 2018 Asociación Argentina de Mecánica Computacional http://www.amcaonline.org.ar